ACS OMEGA

Article

Cite This: ACS Omega 2018, 3, 8803−8812

http://pubs.acs.org/journal/acsodf

Coprecipitation Reaction System Synthesis and Lithium-Ion Capacitor Energy Storage Application of the Porous Structural Bimetallic Sulfide $CoMoS_4$ Nanoparticles

Yun-Kai Wang,[†] Wei-Bin Zhang,[†] Yue Zhao,[†] Kai Li,[†] and Ling-Bin Kong*[,†,‡]

[†]State Key Laboratory of Advanced Processing and Recycling of Non-Ferrous Metals and [‡]School of Materials Science and Engineering, Lanzhou University of Technology, Lanzhou 730050, China

Supporting Information

ABSTRACT: Lithium-ion capacitors (LICs) are noticed as a new-type of energy storage device with both capacitive mechanism and battery mechanism. The LICs own outstanding power density and energy density. In our work, an LIC was constructed by using a simple method to prepare a bimetallic sulfide of $CoMoS_4$ nanoparticles as the anode and a self-made biochar [fructus cannabis's shells (FCS)] with excellent specific surface area as the cathode. The $CoMoS_4$//FCS LIC demonstrated that the range of energy density is from 10 to 41.9 W h/kg and the range of power density is from 75 to 3000 W/kg in the meantime, and it also demonstrated a remarkable cycling performance with the capacitance retention of 95% after 10 000 cycles of charging−discharging at 1 A/g. The designed $CoMoS_4$//FCS LIC device exhibits a superior electrochemical performance because of the $CoMoS_4$ loose porous structure leading to excellent dynamic performance, which is conducive to the diffusion of electrolyte and lithium ion transport, and good electric double layer performance of biochar with large specific surface area could be achieved. Therefore, this bimetallic sulfide is a promising active material for LICs, which could be applied to electric vehicles in the future.

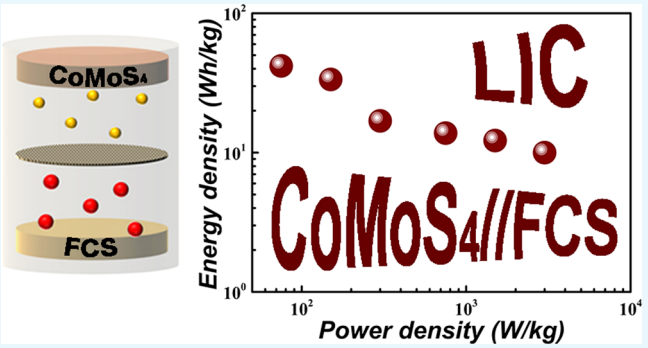

INTRODUCTION

The rapid development of today's society has led to the inability of energy to meet the needs of human. Also, the current energy systems mainly include coal, oil, and natural gas, while the clean energy accounts for a small proportion, such as solar energy, geothermal energy, tidal energy, and so on. This unreasonable proportion of the status has seriously affected the development of mankind. Thus, we must change the irrational current situation. For traditional energy resources, they are nonrenewable, limited, and accompanied with serious environmental pollution. The clean energy resources possess many advantages compared with the former. Therefore, it is necessary to develop an eco-friendly and reusable energy resources to meet the energy needs of the future society. On one hand, the rapid development and ubiquitous use of the large-scale application apparatus demand energy storage equipment; on the other hand, high energy and large power energy storage devices have become the key to mass production of electric vehicles (EVs). Among the energy storage devices, electrochemical energy storage equipment stand out because of their excellent electrochemical performances, such as eco-friendly, outstanding rate capability, and convenient portability.[1]

For the current electrochemical energy-storage systems, lithium-ion batteries (LIBs) and supercapacitors (SCs) have been attracting increasing attention because of their wide use in our social activities.[2,3] From the perspective of energy storage mechanism, the energy storage mechanism of the electric energy conversion of SCs (electrochemical capacitors) is realized by establishing an electric double layer at the interface between the electrode and the electrolyte. Nevertheless, LIB oxidation−reduction reactions of the interface are to achieve energy storage.[4] In terms of actual electrochemical performance, LIBs deliver higher energy density (150−200 W h/kg) but lower power density, while SCs provide higher power density (2−5 kW/kg) and excellent cycle life but lower energy density.[5−7] In consequence, it is a meaningful try to design a kind of electrochemical energy storage device capable of both higher energy and higher power. On the basis of the concept of hybridization, a new-type of storage device with advantages of LIBs and SCs, the discovery of lithium-ion capacitor (LIC) has attracted much attention.[8−10]

The LIC is a hybrid mechanism energy storage device, also known as lithium-ion hybrid capacitor. This hybrid system combines the advantages of the SCs and the LIBs to make up for the Ragone curve with large energy density and large power density of the electrochemical energy storage device vacancies.[11−13] LICs usually consist of a LIB-type anode and

Received: June 21, 2018
Accepted: July 25, 2018
Published: August 8, 2018

DOI: 10.1021/acsomega.8b01408
ACS Omega 2018, 3, 8803−8812

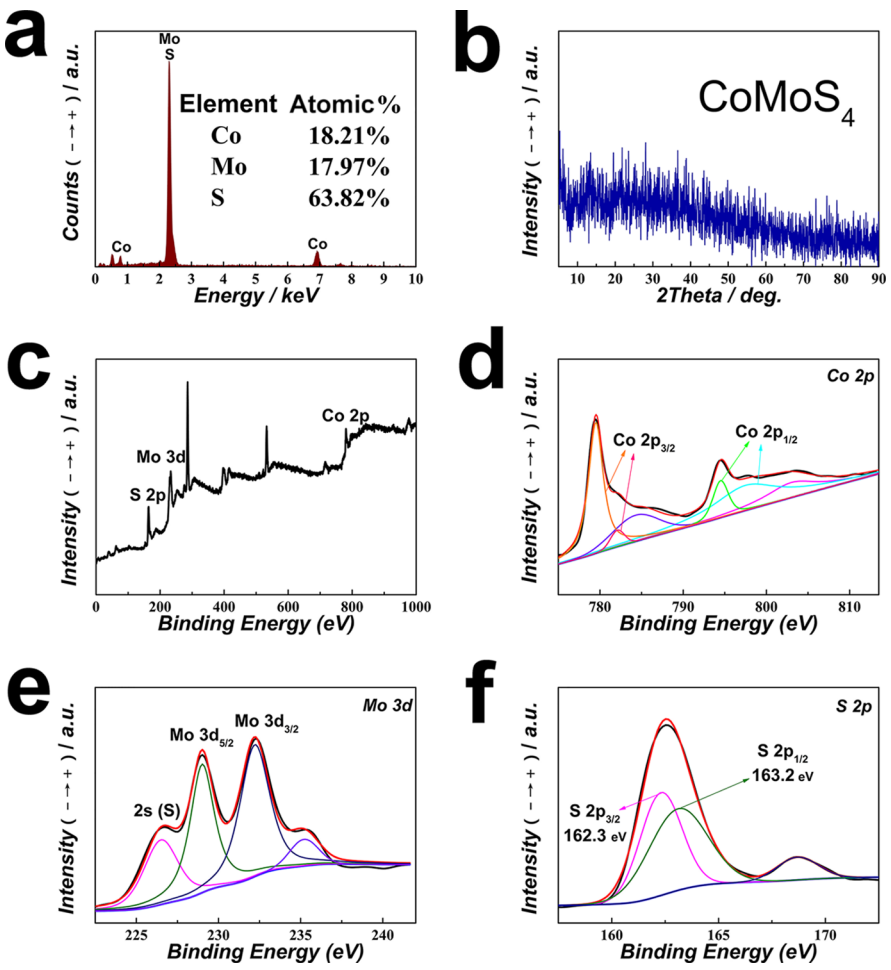

Figure 1. (a) EDS spectrum of $CoMoS_4$ nanoparticles. (b) XRD patterns of $CoMoS_4$ nanoparticles. (c) XPS survey spectrum. (d) Co 2p, (e) Mo 3d, and (f) S 2p spectra of $CoMoS_4$ nanoparticles.

a SC-type cathode, while the advantages of this design are that a combination of rapid charging and discharging of the capacitor-type material and a large capacity of battery-type material characteristics.[14−16] During the operation of the LICs, the adsorption/desorption of hexafluorophosphate ions (PF_6^-) occurs in the positive electrode, while the intercalation/de-intercalation of the cation occurs on the negative electrode.[17−19] This hybrid capacitor combines the advantages of SCs and LIBs, and the actual performance exhibited is closer to ethylene carbonates (ECs).[20] The potential merits of (LIC) will be more apparent in the area of future energy storage devices.

Research into this hybrid LIC started in 2001 when Amatucci and his colleagues first constructed devices that use $Li_4Ti_5O_{12}$ as the anode and cheap commercial activated carbon (AC) as the cathode.[21] Since then, various new materials have been used in the negative and positive materials of such hybrid systems. There are also differences in the performance of LICs constructed from different materials. Generally, LIC positive materials mainly use porous carbon materials that possess excellent specific surface area. AC becomes frequently used positive material because of its specific surface area and lower cost. In LICs, there are three types positive materials in the light of the mechanisms. The first type is insertion material. $LiTi_2(PO_4)_3$,[22] $LiCrTiO_4$,[23] $Li_2Ti_3O_7$,[24] and TiP_2O_7[25] are as examples. The second type is conversion material such as (Fe_2O_3,[26] V_2O_5,[27] TiO_2,[63] and Nb_2O_5[28]). The third type is alloying material incorporating dome-patterned silicon/copper[29] and B−Si/SiO_2/C.[30] Although as traditional battery-type electrode materials, insertion-type positive has excellent structural stability, low specific capacity limits performance of energy density of LICs.[31] However, the conversion metal oxide with pseudocapacitive behavior is considered to be a better selection by reason of its large theoretical capacity (500−1000 mA h/g), outstanding high-power performance, and reliable cycle stability. However, this type shows poor electrical conductivity, which needs to be overcome in application of LICs. Recently, metal nitride vanadium nitride[32] and metal carbide titanium carbide (TiC)[33] have been regarded as prospective LIC positive materials because of their good electrical conductivity and rich oxidation−reduction reaction valence state. This trend indicates that other transition metal compounds are used as positive materials for LICs, showing that there is room for further development. For the time being, transition metal sulfides are identified as prospective electrode materials because of their higher theoretical capacity, and materials such as Co_9S_8[34] and Ni_3S_2[35] have been used in batteries and SCs. For LIC materials, transition metal sulfide is relatively rare, such as $CoNi_2S_4$[36] and TiS_2.[37] This type of material has a space for development in the LIC.

In our work, we adopted the coprecipitation reaction system to prepare $CoMoS_4$ nanoparticles as the anode because a bimetallic sulfide has richer redox reactions and higher

DOI: 10.1021/acsomega.8b01408
ACS Omega 2018, 3, 8803−8812

electrical conductivity than single metal sulfides. The literature has reported that $CoMoS_4$ is used as an SC electrode material and got a specific capacity.[38] We performed a series of physical and chemical properties experiments as well as electrochemical tests to prove that its properties make it suitable as the LIC electrode materials. Then, a self-made biochar [fructus cannabis's shells (FCS)] with an environmental friendly, well-pore structure and excellent surface area was used as the cathode. Finally, a button cell was used as a container to construct an LIC to evaluate its actual performance. As described in detail in this report, the $CoMoS_4$//FCS LIC demonstrated that the range of energy density is from 10 to 41.9 W h/kg and the range of power density is from 75 to 3000 W/kg in the meantime. Simultaneously, the capacity retention rate approached 95% after a cycle of 10 000 at 1 A/g.

RESULTS AND DISCUSSION

Figure 1a shows the energy dispersive spectroscopy (EDS) spectra of $CoMoS_4$ nanoparticles, which reveal that the materials consist of 18.21% Co, 17.97% Mo, and 63.82% S. Compared with $CoMoS_4$ (with stoichiometric ratio of 1:1:4), the slight difference of the stoichiometric ratio is due to the weak peak of oxygen about 0.5 keV. Figure 1b shows that the $CoMoS_4$ nanoparticles were determined by powder X-ray diffractometer (XRD), and no diffraction peaks were observed in the pattern, indicating that the as-obtained sample is an amorphous crystal structure, which is in accord with the previous results in the literature.[39−41] Compared to good crystal structure materials, the structure has more channels for lithium ion transport and is conductive to a better capacity characteristics of electrode materials. In order to further figure out the chemical component of the as-obtained $CoMoS_4$ nanoparticles, X-ray photoelectron spectroscopy (XPS) was used to test the samples and the XPS results are shown in Figure 1. The XPS survey spectrum for the as-obtained $CoMoS_4$ nanoparticles (Figure 1c) indicates that the sample consists of Co, Mo, and S elements. That is, the S 2p spectrum (Figure 1f), it can be divided into the two main peaks located at 163.2 and 162.3 eV in the S 2p core level spectrum could be ascribed to S $2p_{1/2}$ and S $2p_{3/2}$ and one satellite peak at 168.7 eV. On the surface, the sulfur ions at poor complexing results in the peak at 162.0 eV, while the trait of metal−sulfur bonds identifies with the ingredient at 163.2 eV.[42] Figure 1e shows the spectrum of Mo 3d. As regards the Mo $3d_{5/2}$, the peak locates at 228.9 eV, while for the S 2s photoelectrons, the peak locates at 226.5 eV.[41] The peak located at 232.2 eV assigns to the Mo $3d_{3/2}$ for $CoMoS_4$, molybdenum is validating that the oxidation state is similar to that in the $(NH_4)_2[Mo^{6+}S_4]$ precursor.[43,44] In addition, the peak at ∼235.1 eV also indicates the existence of molybdenum (Mo^{6+}).[45] Figure 1d shows the spectrum of Co 2p. The Co $2p_{1/2}$ region displayed a peak at 797.5 eV and one satellite peak at 802.9 eV;[46] the peak at 784.3 eV can be assigned to Co^{2+}.[47] Binding energies of 782.1 eV in the Co 2p core level spectrum can be attributed to Co $2p_{3/2}$. In the $CoMoS_4$ nanoparticles, in a sulfidic environment, the mutual effect of Co atoms and Mo species (Co−Mo−S species) is identified with the peaks at 779.5 and 794.1 eV.[41] Moreover, the Co $2p_{3/2}$ binding energy of 779.5 eV is higher than the Co_9S_8 binding energy value and approaches the Co−Mo−S phase,[38,48] suggesting that Co^{2+} ions are bonded with MoS_4^{2-},[49] leading to the formation of the $CoMoS_4$ phase.[50] The above test results show that the sample composition is close to $CoMoS_4$; the following equations show the forming process of $CoMoS_4$ nanoparticles[39]

$$(NH_4)_2MoS_4 + CoCl_2{\cdot}6H_2O \rightarrow CoMoS_4 + 2NH_4Cl + 6H_2O \quad (1)$$

Figure 2a,b shows the scanning electron microscopy (SEM) images of the interconnecting nanoparticles are the $CoMoS_4$

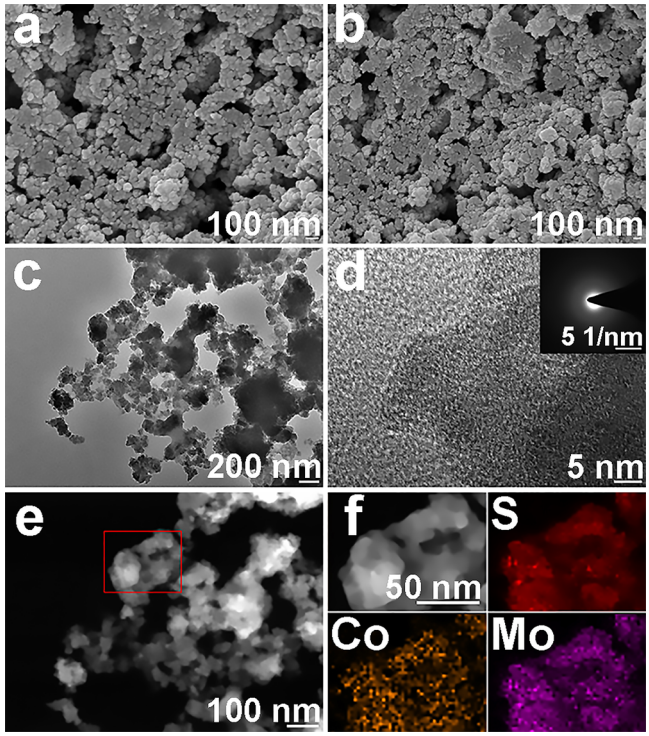

Figure 2. SEM images of (a,b) $CoMoS_4$, TEM images of (c,d) $CoMoS_4$, (e) STEM image, and (f) corresponding elemental mapping images of $CoMoS_4$.

sample with a loosely packed porous structure. It can be seen that the size of nanoparticles ranges from 10 to 100 nm in Figure 2b. This structure is in accord with the results of the transmission electron microscopy (TEM) image in Figure 2c. This loose porous structure has good kinetic properties, which is conducive to the diffusion of electrolyte and lithium ion transport. The high multiples of TEM in Figure 2d and the selected-area electron diffraction illustrations also confirm the structure of $CoMoS_4$ is amorphous, and result also corresponds to the XRD pattern. The selected area of Figure 2e shows the typical scanning transmission electron microscopy (STEM) image and the corresponding elemental mapping images of the $CoMoS_4$ sample; Figure 2f shows that Co, Mo, and S atoms are uniformly distributed in the selected area.

Half-cell assemblies were used to evaluate the electrochemical performance of a single electrode ($CoMoS_4$ and FCS). The $CoMoS_4$ electrode was subjected to a stable prelithiation process by charge−discharge cycle at a current density of 0.1 A/g in a Li half-cell until the capacity reached a stable level. The cyclic voltammetry (CV) curves of the half-cell (prelithiated $CoMoS_4$/Li metal) with a scan rate between 0.1 and 10 mV/s are shown in Figure 3a. Cathodic and anodic peaks appear in the vicinity of 1.3 and 1.5 V, reflecting the Li^+ insertion/extraction processes in charging and discharging

DOI: 10.1021/acsomega.8b01408
ACS Omega 2018, 3, 8803−8812

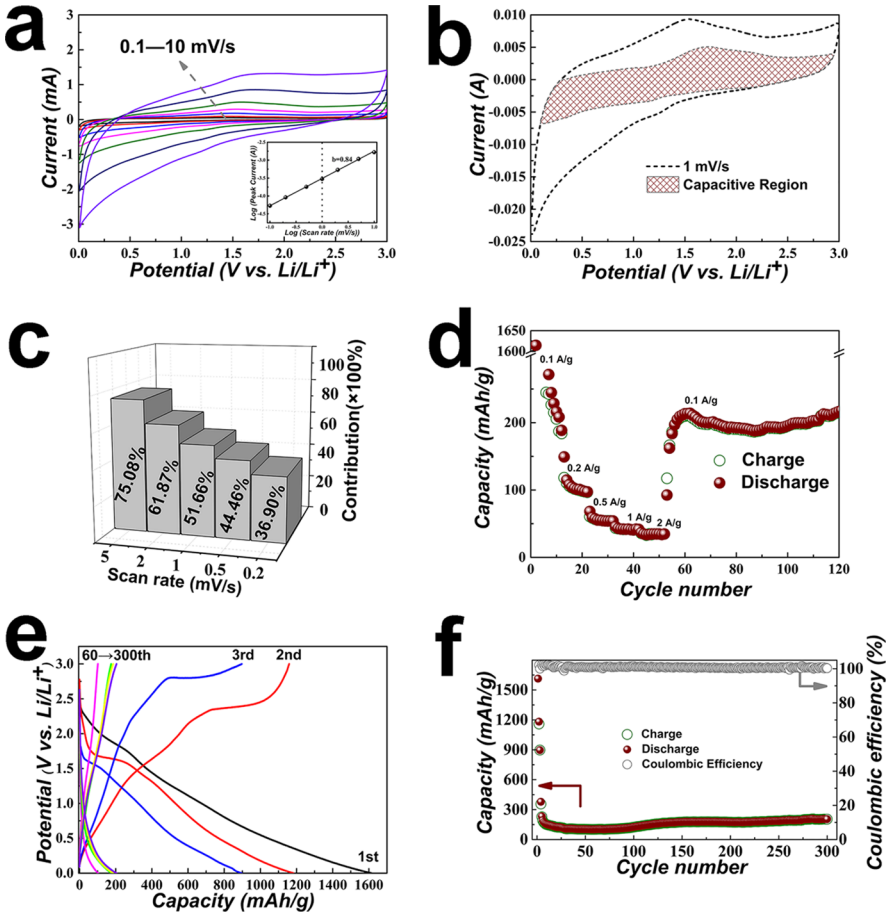

Figure 3. (a) CV curves of $CoMoS_4$ at various scan rates. The inset is *b*-value determination of the peaks in CV curves. (b) Capacitive contribution at 1 mV/s for the $CoMoS_4$ electrode. (c) Contribution ratio of the capacitive at different scan rates for the $CoMoS_4$ electrode. (d) Rate performance of $CoMoS_4$. (e) Discharge−charge curves of the $CoMoS_4$ electrode at different current densities. (f) Long cycling performance of $CoMoS_4$ at the current density of 0.1 A/g.

processes. This trend is similar to the previously reported pseudocapacitive material in the potential range from 0.01 to 3 V (vs Li/Li^+),[36] discussing the lithium ion capacitance where the contribution of the capacitive is extremely important for pseudocapacitive materials. The following quantitative analysis of capacitance contribution was made by the method from Dunn and co-workers.[51,52] Usually, the current and scan rate satisfy the following relationship

$$i = av^b \tag{2}$$

where both *a* and *b* are adjustable values, *i* is the current, and *v* is the sweep rate. The sweep rate in logarithm and plotting current can be used to calculate *b*-value. Different *b*-value has its designated currently reactive control, the semi-infinite linear diffusion presents *b*-value of 0.5, while surface control presents *b*-value of 1. The *b*-value of $CoMoS_4$ electrode peaks is 0.84 with a scan rate between 0.1 and 10 mV/s in illustration of Figure 1a. *b*-Value is much closer to 1 to indicate that the material exhibits mainly pseudocapacitive characteristics. In order to further explore the contribution of capacitance under the different current density, the current was divided into pseudocapacitive effects (k_1v) and diffusion-controlled insertion ($k_2v^{1/2}$).[53] The corresponding equation is

$$i(V) = k_1v + k_2v^{1/2} \tag{3}$$

v denoted in the equation is the sweep rate, while the current can be distinguished two fractions arising from Li^+ insertion and that from capacitive processes by determining both k_1 and k_2. Figure 3b demonstrates the CV profile that has the shaded area representing the contribution of pseudocapacitance at the scan rate of 1 mV/s, which accounts for 51.66% of the total. As shown in Figure 3c, the pseudocapacitance contribution ratios are 36.9, 44.6, 51.66, 61.87, and 75.08% at scan rates of 0.2, 0.5, 1, 2, and 5 mV/s, respectively. The analysis of *b*-value, capacitance contribution rate, and experimental results show that the lithium storage behavior of the $CoMoS_4$ electrode is mainly carried out by the way of pseudocapacitive behavior, which is favorable for fast charge storage and long-term cyclability.[54,55] In order to prove that the $CoMoS_4$ electrode lithium ion storage conduct is a principal pseudocapacitive after the capacity is stable, we have implemented the electrochemical impedance spectroscopy (EIS) tests of the $CoMoS_4$ electrode in half-cell (Figure S1). Charge-transfer resistance (R_{ct}) is about 35 Ω in the light of the high frequency semicircle in Figure S1. Obviously, the slope of the Warburg impedance surpasses 1, which manifests the low frequency curve. The foregoing considerations indicate that influence of diffusion control gets small after the capacity is stable.

Figure 3d shows the rate capability of all $CoMoS_4$ electrodes, when the current density increases from 100, 200, 500, 1000 to 2000 mA/g, the corresponding discharge capacity is 198, 106,

DOI: 10.1021/acsomega.8b01408
ACS Omega 2018, 3, 8803−8812

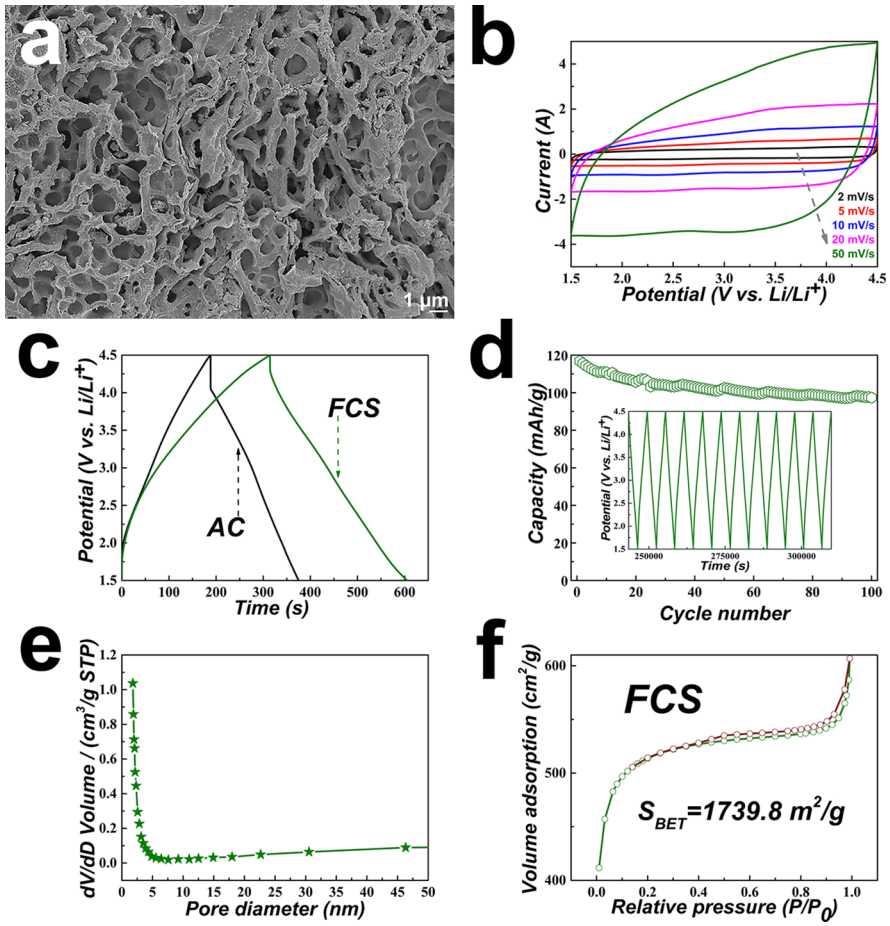

Figure 4. (a) SEM images of FCS, (b) CV curves of FCS at various scan rates, (c) capacitance contrasts of FCS and AC at 1 A/g, (d) cycling performance of FCS at the current density of 0.1 A/g, (e) pore-size distribution plots of FCS, and (f) N_2 adsorption−desorption isotherms.

57, 43, and 34 mA h/g. Finally, when the current density is restored to 100 mA/g, the corresponding discharge capacity also returns to 185 mA h/g. This shows the good capacity reversibility of the $CoMoS_4$ electrode. The galvanostatic charge−discharge curves of the $CoMoS_4$/Li at 0.1 A/g current density in the potential range from 0.01 to 3.0 V (vs Li/Li^+) are presented in Figure 3e. It can be seen that there is no obvious platform after the capacity reaches stability. This proves that the $CoMoS_4$ sample is a pseudocapacitive material. After the first cycle, there is an irreversible capacity loss. The reason for this capacity loss may be due to other side reactions.[56] Figure 3f presents the cyclic curves at 0.1 A/g. Figure 3e,f shows an interesting phenomenon: from the second cycle to the 60th cycles, the capacity dropped from 1200 to 100 mA h/g, but after 60th cycles it increased. On the 150th cycles, the capacity reached 185 mA h/g and remained stable and then rose again. Additionally, the coulombic efficiencies of the $CoMoS_4$ reached to 100%. The increase of capacity during cycling might be attributed to the improved Li-ion diffusion kinetics by a gradual activation process and reversible reactions between metal particles and electrolytes, which has also been observed with several other anode materials.[57−61]

Figure 4a is the SEM image of the FCS sample, the sample shows a highly connected porous structure, similar to coral. This structure provides space for diffusion and transport of electrolyte ions and improves the storage of surface charges. In reality, what is much crucial to the electric double layer capacitors (EDLCs) performance is that the interconnected pores are very adaptive for the electrolyte ion adsorption and diffusion.[62] Figure 4b shows the CV curve of a half-cell device (FCS/Li metal) in the potential range between 1.5 and 4.5 V (vs Li/Li^+). It can be seen that the pattern is an approximately rectangular shape at all scan rates, which indicates that the FCS electrode is mainly EDLC and contains a small amount of pseudocapacitor behavior. The source of pseudocapacitance behavior is due to the small amount of impurity atoms contained in the FCS feedstock. From the charge and discharge curves of FCS and commercial AC at the current densities of 1 A/g shown in Figure 4c, obvious contrast between the two can be seen that the capacity of FCS (100 F/g) is almost double that of AC (63 F/g). Also, the discharge capacity remains essentially unchanged after the 100th cyclic curves at the current density of 0.1 A/g as shown in Figure 4d. Even after 1000 cycles, the discharge capacity remained good (Figure S2). At the same time, we showed the rate capability of the cathode: when the current density increases from 100, 200, 500, 1000 to 2000 mA/g, the corresponding discharge capacity is 110, 100, 90, 80, and 75 mA h/g (Figure S3). The nitrogen adsorption and desorption isotherms were tested at −196 °C to further understand the pore structure of this sample. The isotherm with a distinct hysteresis loop shown in Figure 4f and the pore-size distribution plots shown in Figure 4e consistently indicate that this sample contains some mesopores and macropores and many micropores. The adsorption data were calculated by the standard Brunauer−Emmett−Teller method; therefore, the specific surface area is 1739.8 m^2/g.

DOI: 10.1021/acsomega.8b01408
ACS Omega 2018, 3, 8803−8812

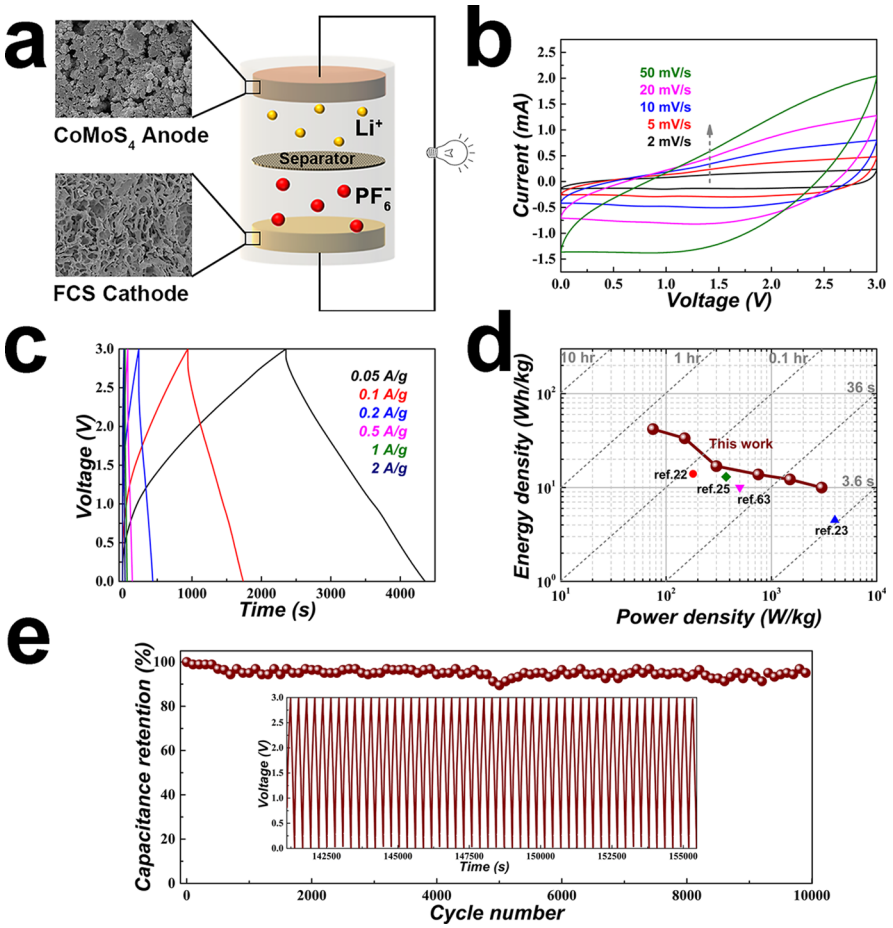

Figure 5. (a) Schematic of the LIC based on FCS cathode and $CoMoS_4$ anode, (b) CV curves of $CoMoS_4$//FCS LIC at different scan rates range from 2 to 50 mV/s, (c) galvanostatic charge−discharge curves of $CoMoS_4$//FCS LIC at different current densities, (d) Ragone plot of $CoMoS_4$//FCS LIC with scattered points designate the data of LICs taken from the literature, and (e) long-term cycle performance of $CoMoS_4$//FCS LIC.

In order to assemble a large-voltage window and a large-energy-density LIC, the charges of the positive and the negative should be balanced ($Q_{anode} = Q_{cathode}$). The key to ensuring the balance of charge is the quality matching of the anode and cathode active materials. The equation $Q = C{\cdot}m$ displays that mass (m) and the stored charge associate with the specific capacity (C) of the electrode, so the mass ratio of the anode and cathode electrodes can be calculated by the following equation:

$$C_{anode} \times \Delta V_{anode} \times m_{anode} = C_{cathode} \times \Delta V_{cathode} \times m_{cathode} \quad (4)$$

ΔV and C are the potential window during charge and discharge of the cathode and anode, respectively, and the specific capacitances, m is the mass. In $CoMoS_4$//FCS, this charge balance is achieved by controlling the mass of the positive and negative active materials by mass ratio. The stabilized capacity is 185 and 102 mA h/g as shown in Figures 3f and 4d, respectively. Through the capacity ratio, the anode and cathode masses were determined as 0.8 and 1.4 mg. Before assembling LICs, the $CoMoS_4$ electrode was subjected to a stable prelithiation process by charge−discharge cycle at a current density of 0.1 A/g in a Li half-cell until the capacity reached a stable level to obtain a high retention of capacity and ended in a state of charging to 2.01 V (a cross potential of a positive electrode discharge and a negative electrode charge). In the same way, the FCS electrode was pre-activated for 10 cycles and ended in a state of discharging to 2.01 V (Figure S5). After that, the equipotential prelithiated anode ($CoMoS_4$) and the activated cathode (FCS) were assembled into an LIC in the form of a button cell in a nitrogen glovebox. The composition of the $CoMoS_4$//FCS LIC device is shown in Figure 5a, prelithiated $CoMoS_4$ is used as a anode and activated FCS as a cathode in 1 mol $LiPF_6$ in EC/dimethyl carbonate (DMC)/ethyl methyl carbonate (EMC) (1:1:1) electrolyte solution.

The CV curves of $CoMoS_4$//FCS LIC are exhibited in Figure 5b. The different scan rate CV curves at 2−50 mV/s exhibit a shape that is different from the perfect rectangle of a traditional symmetric type SC due to the different energy storage mechanisms of the positive and negative, the homologous voltage testing window was chosen between 0 and 3 V. As shown in Figure 5c, the galvanostatic charge−discharge curves are at different current densities. It can be seen that the curves presents an approximate isosceles triangle. This linear slope is expected for hybrid capacitor. The mass specific capacitance (C) was calculated using formula $C = i{\cdot}t/m{\cdot}\Delta V$, where i is the applied current, t is the discharge time, ΔV is the potential difference (not including the ohmic drop), and m is the total mass of the two electrode. At the current densities of 0.05, 0.1, 0.2, 0.5, 1, and 2 A/g, the device exhibits a capacity of 33.5, 26.75, 13.5, 11, 9.75, and 8 F/g, respectively. Electrochemical impedance spectroscopy (EIS) was used to characterize the $CoMoS_4$//FCS LIC (Figure S4). R_s presents

DOI: 10.1021/acsomega.8b01408
ACS Omega 2018, 3, 8803−8812

the resistance of cell components and electrolyte, R_s of the $CoMoS_4$//FCS LIC was estimated to be 7 Ω. Charge-transfer resistance (R_{ct}) is about 39 Ω in the light of the high frequency semicircle in Figure S1. Obviously, the slope of the Warburg impedance surpasses 1, which manifests the low frequency curve. The foregoing considerations indicate that electrolyte ions can diffuse rapidly into this loose porous structure of $CoMoS_4$ nanoparticles.[64]

Figure 5d shows the Ragone plots of $CoMoS_4$//FCS LICs. The energy and power density of the LIC were calculated using the following equations:

$$E = \frac{1}{2}\cdot C\cdot (V)^2 \quad (5)$$

$$P = E/t \quad (6)$$

$$\Delta V = V_{max} - V_{min} \quad (7)$$

where t is the discharge time, V_{max} and V_{min} are the upper and lower voltages during the charge−discharge process, and C is the mass specific capacitance. The $CoMoS_4$//FCS LIC exhibited highest power density and energy density in the LICs. Particularly, the $CoMoS_4$//FCS LIC demonstrated that the range of energy density is from 10 to 41.9 W h/kg and the range of power density is from 75 to 3000 W/kg in the meantime (Table 1). Even more noteworthy is the cycling performance of the $CoMoS_4$//FC LIC. In Figure 5e, the capacity retention rate approached 95% after a cycle of 10 000 at 1 A/g. The $CoMoS_4$//FCS LIC device exhibiting a superior electrochemical performance is due to the fact that $CoMoS_4$ loose porous structure has excellent dynamic performance, which is conducive to the diffusion of electrolyte and lithium ion transport. Also, good electric double layer performance of biochar with high specific surface area could be achieved. Therefore, this bimetallic sulfide is a promising active material for LICs, which could be applied to EVs in the future.

Table 1. LICs Performances Reported in the Previous Literature Studies

anode//cathode	voltage range (V)	energy density (W h/kg)	power density (W/kg)	cycling life
$LiTi_2(PO_4)_3$//AC[22]	0−3	14	180	46% @ 1000 cycles
$LiCrTiO_4$//AC[23]	1−2.5	4.5	4000	84% @ 1000 cycles
TiP_2O_7//AC[25]	0−3	13	371	100% @ 500 cycles
TiO_2−B//AC[63]	0−3	10	500	100% @ 1000 cycles
this work	0−3	41.9−10	75−3000	95% @ 10 000 cycles

CONCLUSIONS

In summary, the interconnecting nanoparticles of the $CoMoS_4$ sample with a loosely packed porous structure were fabricated with a simple chemical coprecipitation method as the LIC anode material. Meanwhile, a self-made biochar (FCS) with an environmental friendly, well-pore structure and excellent surface area were used as the cathode materials. In this, the LIC ($CoMoS_4$//FCS) with considerable performance was designed and manufactured by the prelithiated $CoMoS_4$ anode and the FCS cathode. The consequences uncover that this structure of $CoMoS_4$ nanoparticles has more lithium ion transport channels and considerable contribution of pseudocapacitance is conductive to better capacity characteristics of electrode materials, and well-pore structure of FCS excellent surface area provides space for diffusion and transport of electrolyte ions and optimizes the storage of surface charges. Moreover, the $CoMoS_4$//FCS LIC demonstrated that the range of energy density is from 10 to 41.9 W h/kg and the range of power density is from 75 to 3000 W/kg in the meantime. Simultaneously, the capacity retention rate approached 95% after a cycle of 10 000 at 1 A/g. Therefore, this bimetallic sulfide is a promising active material for LICs, which could be applied to EVs in the future.

EXPERIMENT SECTION

Preparation of the $(NH_4)_2MoS_4$ Precursor. All the chemicals have been used in this work were of analytical grade, which can be directly used after purchase. It was a typical synthesis procedure that 12.5 g of $(NH_4)_6Mo_7O_{24}$ was dissolved in 30 mL of deionized water into a three-necked flask with vigorous stirring, then adding 15 mL ammonia water into the three-necked flask under vigorous stirring. With that, 113 mL of $(NH_4)_2S$ solution (S % = 8 wt %) was then added to this solution and the mixture was further maintained at 70 °C for 2 h. The product was cooled to room temperature, crystallized for 12 h, and then rinsed with anhydrous ethanol and deionized water many times. Finally, the samples were dried at room temperature for 12 h to obtain $(NH_4)_2MoS_4$. The mechanism of preparing the $(NH_4)_2MoS_4$ crystal can be expressed as eqs 8 and 9

$$(NH_4)_6Mo_7O_{24} + 8NH_3\cdot H_2O \rightarrow 7(NH_4)_2MoO_4 + 4H_2O \quad (8)$$

$$(NH_4)_2MoO_4 + 4(NH_4)_2S \rightarrow (NH_4)_2MoS_4 + 4NH_3\cdot H_2O \quad (9)$$

Preparation of $CoMoS_4$ Nanoparticles. The $CoMoS_4$ nanoparticles were synthesized by the coprecipitation reaction system. $CoCl_2\cdot 6H_2O$ (0.5 g) and 0.6 g of the as-prepared $(NH_4)_2MoS_4$ were dissolved in 60 mL of deionized water under vigorous stirring, and the mixed solution of the reaction was kept at 70 °C for 2 h. After that, the precipitate was cooled to room temperature, then rinsed with anhydrous ethanol and deionized water many times, and dried at 60 °C. The sample was further calcined at 200 °C for 3 h in N_2 and the heating rate of 2 °C/min to obtain $CoMoS_4$ nanoparticles.

Preparation of Porous Carbon. The porous carbon was prepared by carbonizing the precursor of FCS. First, the dried FCS was pre-carbonized at 300 °C for 3 h in a chamber furnace under air atmosphere. Second, 3 g of both FCSs and KOH were mixed into a beaker with vigorous stirring at room temperature for 2 h, and next, the product was dried at 80 °C for 12 h. Third, under N_2 flow of 60 mL min^{-1} at 700 °C for 2 h and the heating rate of 2 °C/min, the product was activated from the second step and then was cooled to indoor temperature automatically. Finally, the samples were rinsed with deionized water and 1 mol/L HCl many times until the pH = 7 and dried at 80 °C for 12 h in vacuum to obtain FCS.

Characterization of Materials. The $CoMoS_4$ nanoparticles were determined by power X-ray diffraction measurements (XRD, Rigaku, D/Max 2400, Japan). The element content and uniform distribution of $CoMoS_4$ nanoparticles

DOI: 10.1021/acsomega.8b01408
ACS Omega 2018, 3, 8803−8812

were investigated EDS. TEM (JEOL, JEM-2010, Japan) analyzed the microstructure of $CoMoS_4$ nanoparticles. Furthermore, the element components of $CoMoS_4$ nanoparticles were assessed by XPS (ESCALAB 250Xi). The microscopic morphology and structure were observed by SEM (JEOL, JSM-6701F, Japan).

Electrochemical Measurements. The electrodes of $CoMoS_4$ and the FCS preparation process are as follows: active material ($CoMoS_4$ or FCS) (80 wt %), conductive agent (acetylene black) (10 wt %), and the binder (poly vinylidene fluoride) (10 wt %) were mixed in *N*-methyl pyrrolidone to form a slurry, and the slurry was coated uniformly on the clean copper/aluminum foil collector (copper foils and aluminum foils correspond to the $CoMoS_4$ anodes and the FCS cathodes, respectively). Then, the electrode was dried in a drying cabinet at 60 °C for 8 h and then was transferred to a vacuum drying chamber at 60 °C for 12 h. The mass loading of $CoMoS_4$ and FCS coated each circular electrode, which was cut into 14 mm diameter range from 0.6 to 1.4 mg. The lithium metal piece was regarded as reference electrode and counter electrode; the electrolyte composed of 1 mol $LiPF_6$ in EC/EMC/DMC mixture (1:1:1 v/v/v) and Celgard 2400 as the separator. The cell was done in a glovebox which was full of argon (Ar). Moreover, the oxygen content of the glovebox was less than 1 ppm, and the moisture content was less-than 0.1 ppm. The hybrid LIC was tested the same as the half cells. The cycling measurements and the galvanostatic discharge−charge performance were tested by the Land testing system (CT-2001A). CV characteristics of LIC cell and half-cell were measured by using the Electrochemical Workstation (CHI660D, Shanghai, China). The potential range of half cells was between 0.01 and 3.00 V, and the hybrid LIC was conducted with the voltage window 0−3 V.

■ ASSOCIATED CONTENT

Supporting Information

The Supporting Information is available free of charge on the ACS Publications website at DOI: 10.1021/acsomega.8b01408.

Nyquist plot of the $CoMoS_4$ electrode; cycling performance of FCS (cycling performance of 1000 cycles); rate performance of the FCS electrode; Nyquist plot of $CoMoS_4$//FCS LIC; and typical FCS electrode discharge curve and $CoMoS_4$ electrode charge curve based $CoMoS_4$//FCS LIC recorded at the current density of 0.1 A/g (PDF)

■ AUTHOR INFORMATION

Corresponding Author

*E-mail: konglb@lut.cn. Phone: +86 931 2976579. Fax: +86 931 2976578 (L.-B.K.).

ORCID

Ling-Bin Kong: 0000-0002-2271-4202

Notes

The authors declare no competing financial interest.

■ ACKNOWLEDGMENTS

This work was supported by the National Natural Science Foundation of China (no. 51762031) and the Foundation for Innovation Groups of Basic Research in Gansu Province (no. 1606RJIA322).

■ REFERENCES

(1) Armand, M.; Tarascon, J.-M. Building better batteries. *Nature* **2008**, *451*, 652−657.

(2) Xia, Q.; Yang, H.; Wang, M.; Yang, M.; Guo, Q.; Wan, L.; Yu, Y. High Energy and High Power Lithium-Ion Capacitors Based on Boron and Nitrogen Dual-Doped 3D Carbon Nanofibers as Both Cathode and Anode. *Adv. Energy Mater.* **2017**, *7*, 1701336.

(3) Dubal, D. P.; Ayyad, O.; Ruiz, V.; Gómez-Romero, P. Hybrid energy storage: the merging of battery and supercapacitor chemistries. *Chem. Soc. Rev.* **2015**, *44*, 1777−1790.

(4) Zhang, W.-B.; Ma, X.-J.; Kong, L.-B. Nanocrystalline Intermetallic Tungsten Carbide: Nanoscaled Solidoid Synthesis, Nonfaradaic Pseudocapacitive Property, and Electrode Material Application. *Adv. Mater. Interfaces* **2017**, *4*, 1700099.

(5) Gu, H.; Zhu, Y.-E.; Yang, J.; Wei, J.; Zhou, Z. Nanomaterials and Technologies for Lithium-Ion Hybrid Supercapacitors. *ChemNanoMat* **2016**, *2*, 578−587.

(6) Ma, Y.; Chang, H.; Zhang, M.; Chen, Y. Graphene-based materials for lithium-ion hybrid supercapacitors. *Adv. Mater.* **2015**, *27*, 5296−5308.

(7) Li, B.; Dai, F.; Xiao, Q.; Yang, L.; Shen, J.; Zhang, C.; Cai, M. Activated Carbon from Biomass Transfer for High-Energy Density Lithium-Ion Supercapacitors. *Adv. Energy Mater.* **2016**, *6*, 1600802.

(8) Brandt, A.; Balducci, A. A study about the use of carbon coated iron oxide-based electrodes in lithium-ion capacitors. *Electrochim. Acta* **2013**, *108*, 219−225.

(9) Ren, J. J.; Su, L. W.; Qin, X.; Yang, M.; Wei, J. P.; Zhou, Z.; Shen, P. W. Pre-lithiated graphene nanosheets as negative electrode materials for Li-ion capacitors with high power and energy density. *J. Power Sources* **2014**, *264*, 108−113.

(10) Park, M.-S.; Lim, Y.-G.; Kim, J.-H.; Kim, Y.-J.; Cho, J.; Kim, J.-S. A Novel Lithium-Doping Approach for an Advanced Lithium Ion Capacitor. *Adv. Energy Mater.* **2011**, *1*, 1002−1006.

(11) Simon, P.; Gogotsi, Y. Materials for electrochemical capacitors. *Nat. Mater.* **2008**, *7*, 845−854.

(12) Hall, P. J.; Mirzaeian, M.; Fletcher, S. I.; Sillars, F. B.; Rennie, A. J. R.; Shitta-Bey, G. O.; Wilson, G.; Cruden, A. Energy storage in electrochemical capacitors: designing functional materials to improve performance. *Energy Environ. Sci.* **2010**, *3*, 1238−1251.

(13) Amaresh, S.; Karthikeyan, K.; Jang, I.-C.; Lee, Y. S. Single-step microwave mediated synthesis of the CoS2 anode material for high rate hybrid supercapacitors. *J. Mater. Chem. A* **2014**, *2*, 11099−11106.

(14) Naoi, K.; Naoi, W.; Aoyagi, S.; Miyamoto, J.-i.; Kamino, T. New Generation "Nanohybrid Supercapacitor". *Acc. Chem. Res.* **2012**, *46*, 1075−1083.

(15) Aravindan, V.; Gnanaraj, J.; Lee, Y.-S.; Madhavi, S. Insertion-type electrodes for nonaqueous Li-ion capacitors. *Chem. Rev.* **2014**, *114*, 11619−11635.

(16) Zhao, Y.; Cui, Y.; Shi, J.; Liu, W.; Shi, Z.; Chen, S.; Wang, X. Two-dimensional biomass-derived carbon nanosheets and MnO/carbon electrodes for high-performance Li-ion capacitors. *J. Mater. Chem. A* **2017**, *5*, 15243−15252.

(17) Wang, K.; Wang, N.; He, J.; Yang, Z.; Shen, X.; Huang, C. Graphdiyne Nanowalls as Anode for Lithium-Ion Batteries and Capacitors Exhibit Superior Cyclic Stability. *Electrochim. Acta* **2017**, *253*, 506−516.

(18) Wu, M.-S.; Wang, C.; Jow, J.-J. Self-assembly of one-dimensional nitrogen-doped hollow carbon nanoparticle chains derived from zinc hexacyanoferrate coordination polymer for lithium-ion capacitors. *Electrochim. Acta* **2016**, *222*, 856−861.

(19) Pazhamalai, P.; Krishnamoorthy, K.; Sudhakaran, M. S. P.; Kim, S. J. Fabrication of High-Performance Aqueous Li-Ion Hybrid Capacitor with LiMn2 O4 and Graphene. *ChemElectroChem* **2017**, *4*, 396−403.

(20) Zheng, J.-S.; Zhang, L.; Shellikeri, A.; Cao, W.; Wu, Q.; Zheng, J. P. A hybrid electrochemical device based on a synergetic inner combination of Li ion battery and Li ion capacitor for energy storage. *Sci. Rep.* **2017**, *7*, 41910.

DOI: 10.1021/acsomega.8b01408
ACS Omega 2018, 3, 8803−8812

(21) Amatucci, G. G.; Badway, F.; Du Pasquier, A.; Zheng, T. An asymmetric hybrid nonaqueous energy storage cell. *J. Electrochem. Soc.* **2001**, *148*, A930−A939.
(22) Aravindan, V.; Chuiling, W.; Reddy, M. V.; Rao, G. V. S.; Chowdari, B. V. R.; Madhavi, S. Carbon coated nano-LiTi2(PO4)3 electrodes for non-aqueous hybrid supercapacitors. *Phys. Chem. Chem. Phys.* **2012**, *14*, 5808−5814.
(23) Aravindan, V.; Chuiling, W.; Madhavi, S. High power lithium-ion hybrid electrochemical capacitors using spinel LiCrTiO4 as insertion electrode. *J. Mater. Chem.* **2012**, *22*, 16026−16031.
(24) Chen, F.; Li, R.; Hou, M.; Liu, L.; Wang, R.; Deng, Z. Preparation and characterization of ramsdellite Li2Ti3O7 as an anode material for asymmetric supercapacitors. *Electrochim. Acta* **2005**, *51*, 61−65.
(25) Aravindan, V.; Reddy, M. V.; Madhavi, S.; Mhaisalkar, S. G.; Subba Rao, G. V.; Chowdari, B. V. R. Hybrid supercapacitor with nano-TiP2O7 as intercalation electrode. *J. Power Sources* **2011**, *196*, 8850−8854.
(26) Karthikeyan, K.; Amaresh, S.; Lee, S. N.; Aravindan, V.; Lee, Y. S. Fluorine-Doped Fe2O3as High Energy Density Electroactive Material for Hybrid Supercapacitor Applications. *Chem.—Asian J.* **2014**, *9*, 852−857.
(27) Chen, Z.; Augustyn, V.; Wen, J.; Zhang, Y.; Shen, M.; Dunn, B.; Lu, Y. High-Performance Supercapacitors Based on Intertwined CNT/V2O5 Nanowire Nanocomposites. *Adv. Mater.* **2011**, *23*, 791−795.
(28) Jia, Z.-Y.; Liu, M.-N.; Zhao, X.-L.; Wang, X.-S.; Pan, Z.-H.; Zhang, Y.-G. Lithium Ion Hybrid Supercapacitor Based on Three-Dimensional Flower-Like Nb_2O_5 and Activated Carbon Electrode Materials. *Acta Phys.-Chim. Sin.* **2017**, *33*, 2510−2516.
(29) Liu, X.; Jung, H.-G.; Kim, S.-O.; Choi, H.-S.; Lee, S.; Moon, J. H.; Lee, J. K. Silicon/copper dome-patterned electrodes for high-performance hybrid supercapacitors. *Sci. Rep.* **2013**, *3*, 3183.
(30) Yi, R.; Chen, S.; Song, J.; Gordin, M. L.; Manivannan, A.; Wang, D. High-Performance Hybrid Supercapacitor Enabled by a High-Rate Si-based Anode. *Adv. Funct. Mater.* **2014**, *24*, 7433−7439.
(31) Lee, C. h.; Xu, F.; Jung, C. Influence of the electrolyte distribution near the micropores of the activated carbon (AC) electrode on high rate performance of high voltage capacitors. *Electrochim. Acta* **2014**, *131*, 240−244.
(32) Lu, X.; Liu, T.; Zhai, T.; Wang, G.; Yu, M.; Xie, S.; Ling, Y.; Liang, Y.; Li, Y. Improving the Cycling Stability of Metal-Nitride Supercapacitor Electrodes with a Thin Carbon Shell. *Adv. Energy Mater.* **2014**, *4*, 1300994.
(33) Zou, G.; Wang, H.; Mara, N.; Luo, H.; Li, N.; Di, Z.; Bauer, E.; Wang, Y.; Burrell, A.; Zhang, X.; Nastasi, M.; Jia, Q. Chemical solution deposition of epitaxial carbide films. *J. Am. Chem. Soc.* **2010**, *132*, 2516−2517.
(34) Luo, W.; Xie, Y.; Wu, C.; Zheng, F. Spherical CoS2@carbon core-shell nanoparticles: one-pot synthesis and Li storage property. *Nanotechnology* **2008**, *19*, 075602.
(35) Yu, W.; Lin, W.; Shao, X.; Hu, Z.; Li, R.; Yuan, D. High performance supercapacitor based on Ni 3 S 2 /carbon nanofibers and carbon nanofibers electrodes derived from bacterial cellulose. *J. Power Sources* **2014**, *272*, 137−143.
(36) Jagadale, A.; Zhou, X.; Blaisdell, D.; Yang, S. Carbon nanofibers (CNFs) supported cobalt-nickel sulfide ($CoNi_2S_4$) nanoparticles hybrid anode for high performance lithium ion capacitor. *Sci. Rep.* **2018**, *8*, 1602.
(37) Chaturvedi, A.; Hu, P.; Aravindan, V.; Kloc, C.; Madhavi, S. Unveiling two-dimensional TiS2 as an insertion host for the construction of high energy Li-ion capacitors. *J. Mater. Chem. A* **2017**, *5*, 9177−9181.
(38) Dai, Y.-H.; Kong, L.-B.; Yan, K.; Shi, M.; Zhang, T.; Luo, Y.-C.; Kang, L. Simple synthesis of a CoMoS4 based nanostructure and its application for high-performance supercapacitors. *RSC Adv.* **2016**, *6*, 7633−7642.
(39) Guo, G.; Song, Z.; Cong, C.; Zhang, K. CoMoS4 Nanoflowers as Anode for Secondary Lithium Batteries. *J. Nanopart. Res.* **2007**, *9*, 653−656.
(40) Sun, Y.; Wang, C.; Ding, T.; Zuo, J.; Yang, Q. Fabrication of amorphous CoMoS4as a bifunctional electrocatalyst for water splitting under strong alkaline conditions. *Nanoscale* **2016**, *8*, 18887−18892.
(41) Polychronopoulou, K.; Malliakas, C. D.; He, J.; Kanatzidis, M. G. Selective Surfaces: Quaternary Co(Ni)MoS-Based Chalcogels with Divalent (Pb2+, Cd2+, Pd2+) and Trivalent (Cr3+, Bi3+) Metals for Gas Separation. *Chem. Mater.* **2012**, *24*, 3380−3392.
(42) Chen, H.; Jiang, J.; Zhang, L.; Wan, H.; Qi, T.; Xia, D. Highly conductive NiCo2S4 urchin-like nanostructures for high-rate pseudocapacitors. *Nanoscale* **2013**, *5*, 8879−8883.
(43) Tran, P. D.; Nguyen, M.; Pramana, S. S.; Bhattacharjee, A.; Chiam, S. Y.; Fize, J.; Field, M. J.; Artero, V.; Loo, J.; Barber, J. Copper molybdenum sulfide: a new efficient electrocatalyst for hydrogen production from water. *Energy Environ. Sci.* **2012**, *5*, 8912−8916.
(44) Laurie, S. H.; Pratt, D. E.; Raynor, J. B. The copper-molybdenum antagonism in ruminants. III. Reaction of copper(II) with tetrathiomolybdate(VI). *Inorg. Chim. Acta* **1986**, *123*, 193−196.
(45) Bissett, M. A.; Kinloch, I. A.; Dryfe, R. A. W. Characterization of MoS2-Graphene Composites for High-Performance Coin Cell Supercapacitors. *ACS Appl. Mater. Interfaces* **2015**, *7*, 17388−17398.
(46) Shao, L.; Qian, X.; Wang, X.; Li, H.; Yan, R.; Hou, L. Low-cost and highly efficient CoMoS 4 /NiMoS 4 -based electrocatalysts for hydrogen evolution reactions over a wide pH range. *Electrochim. Acta* **2016**, *213*, 236−243.
(47) Pang, X.; Guo, Y.; Zhang, Y.; Xu, B.; Qi, F. LaCoO 3 perovskite oxide activation of peroxymonosulfate for aqueous 2-phenyl-5-sulfobenzimidazole degradation: Effect of synthetic method and the reaction mechanism. *Chem. Eng. J.* **2016**, *304*, 897−907.
(48) Okamoto, Y.; Ochiai, K.; Kawano, M.; Kobayashi, K.; Kubota, T. Effects of support on the activity of Co-Mo sulfide model catalysts. *Appl. Catal., A* **2002**, *226*, 115−127.
(49) Xu, X.; Song, Y.; Xue, R.; Zhou, J.; Gao, J.; Xing, F. Amorphous CoMoS 4 for a valuable energy storage material candidate. *Chem. Eng. J.* **2016**, *301*, 266−275.
(50) Zheng, X.; Guo, J.; Shi, Y.; Xiong, F.; Zhang, W.-H.; Ma, T.; Li, C. Low-cost and high-performance CoMoS4 and NiMoS4 counter electrodes for dye-sensitized solar cells. *Chem. Commun.* **2013**, *49*, 9645−9647.
(51) Augustyn, V.; Simon, P.; Dunn, B. Pseudocapacitive oxide materials for high-rate electrochemical energy storage. *Energy Environ. Sci.* **2014**, *7*, 1597−1614.
(52) Wang, J.; Polleux, J.; Lim, J.; Dunn, B. Pseudocapacitive Contributions to Electrochemical Energy Storage in TiO2(Anatase) Nanoparticles. *J. Phys. Chem. C* **2007**, *111*, 14925−14931.
(53) Augustyn, V.; Come, J.; Lowe, M. A.; Kim, J. W.; Taberna, P.-L.; Tolbert, S. H.; Abruña, H. D.; Simon, P. High-rate electrochemical energy storage through Li+ intercalation pseudocapacitance. *Nat. Mater.* **2013**, *12*, 518−522.
(54) Shen, L.; Yu, L.; Yu, X.-Y.; Zhang, X.; Lou, X. W. D. Self-Templated Formation of Uniform NiCo2O4Hollow Spheres with Complex Interior Structures for Lithium-Ion Batteries and Supercapacitors. *Angew. Chem., Int. Ed.* **2015**, *54*, 1868−1872.
(55) Xiong, D.; Li, X.; Shan, H.; Yan, B.; Dong, L.; Cao, Y.; Li, D. Controllable oxygenic functional groups of metal-free cathodes for high performance lithium ion batteries. *J. Mater. Chem. A* **2015**, *3*, 11376−11386.
(56) Wu, Z.-S.; Ren, W.; Wen, L.; Gao, L.; Zhao, J.; Chen, Z.; Zhou, G.; Li, F. Graphene Anchored with Co3O4 Nanoparticles as Anode of Lithium Ion Batteries with Enhanced Reversible Capacity and Cyclic Performance. *ACS Nano* **2010**, *4*, 3187−3194.
(57) Hao, Y.; Chen, C.; Yang, X.; Xiao, G.; Zou, B.; Yang, J.; Wang, C. Studies on intrinsic phase-dependent electrochemical properties of MnS nanocrystals as anodes for lithium-ion batteries. *J. Power Sources* **2017**, *338*, 9−16.

DOI: 10.1021/acsomega.8b01408
ACS Omega 2018, 3, 8803−8812

(58) Huang, G.; Zhang, F.; Du, X.; Qin, Y.; Yin, D.; Wang, L. Metal Organic Frameworks Route to in Situ Insertion of Multiwalled Carbon Nanotubes in Co3O4 Polyhedra as Anode Materials for Lithium-Ion Batteries. *ACS Nano* **2015**, *9*, 1592−1599.
(59) Peng, C.; Chen, B.; Qin, Y.; Yang, S.; Li, C.; Zuo, Y.; Liu, S. Facile ultrasonic synthesis of CoO quantum dot/graphene nanosheet composites with high lithium storage capacity. *ACS Nano* **2012**, *6*, 1074−1081.
(60) Wang, D.; Yang, J.; Li, X.; Geng, D.; Li, R.; Cai, M.; Sham, T.-K. Layer by layer assembly of sandwiched graphene/SnO2 nanorod/carbon nanostructures with ultrahigh lithium ion storage properties. *Energy Environ. Sci.* **2013**, *6*, 2900−2906.
(61) Zou, F.; Hu, X.; Li, Z.; Qie, L.; Hu, C.; Zeng, R.; Jiang, Y. MOF-Derived Porous ZnO/ZnFe2O4/C Octahedra with Hollow Interiors for High-Rate Lithium-Ion Batteries. *Adv. Mater.* **2014**, *26*, 6622−6628.
(62) Li, K.; Zhang, W.-B.; Zhao, Z.-Y.; Zhao, Y.; Chen, X.-W.; Kong, L.-B. A porous carbon material from pyrolysis of fructus cannabis's shells for supercapacitor electrode application. *Mater. Res. Express* **2018**, *5*, 025514.
(63) Wang, D.-W.; Fang, H.-T.; Li, F.; Chen, Z.-G.; Zhong, Q.-S.; Lu, G. Q.; Cheng, H.-M. Aligned titania nanotubes as an intercalation anode material for hybrid electrochemical energy storage. *Adv. Funct. Mater.* **2008**, *18*, 3787−3793.
(64) Salvatierra, R. V.; Zakhidov, D.; Sha, J.; Kim, N. D.; Lee, S.-K.; Raji, A.-R. O.; Tour, J. M. Graphene carbon nanotube carpets grown using binary catalysts for high-performance Lithium-ion capacitors. *ACS Nano* **2017**, *11*, 2724−2733.

DOI: 10.1021/acsomega.8b01408
ACS Omega 2018, 3, 8803−8812